J|A|C|S
ARTICLES
Published on Web 03/13/2004

The Nature of the Exchange Coupling between High-Spin Fe(III) Heme o_3 and Cu_B(II) in *Escherichia coli* Quinol Oxidase, Cytochrome bo_3: MCD and EPR Studies

Myles R. Cheesman,*,† Vasily S. Oganesyan,† Nicholas J. Watmough,‡ Clive S. Butler,‡,§ and Andrew J. Thomson*,†

Contribution from the School of Chemical Sciences and Pharmacy and School of Biological Sciences, Centre for Metalloprotein Spectroscopy and Biology (CMSB), University of East Anglia, Norwich NR4 7TJ, U.K.

Received October 3, 2003; E-mail: m.cheesman@uea.ac.uk

Abstract: Fully oxidized cytochrome bo_3 from *Escherichia coli* has been studied in its oxidized and several ligand-bound forms using electron paramagnetic resonance (EPR) and magnetic circular dichroism (MCD) spectroscopies. In each form, the spin-coupled high-spin Fe(III) heme o_3 and Cu_B(II) ion at the active site give rise to similar fast-relaxing broad features in the dual-mode X-band EPR spectra. Simulations of dual-mode spectra are presented which show that this EPR can arise only from a dinuclear site in which the metal ions are weakly coupled by an anisotropic exchange interaction of $|\mathbf{J}| \approx 1$ cm^{-1}. A variable-temperature and magnetic field (VTVF) MCD study is also presented for the cytochrome bo_3 fluoride and azide derivatives. New methods are used to extract the contribution to the MCD of the spin-coupled active site in the presence of strong transitions from low-spin Fe(III) heme *b*. Analysis of the MCD data, independent of the EPR study, also shows that the spin-coupling within the active site is weak with $|\mathbf{J}| \approx 1$ cm^{-1}. These conclusions overturn a long-held view that such EPR signals in bovine cytochrome *c* oxidase arise from an $S' = 2$ ground state resulting from strong exchange coupling ($|\mathbf{J}| > 10^2$ cm^{-1}) within the active site.

1. Introduction

The quinol oxidase cytochrome bo_3 (bo_3[1]), from *Escherichia coli*, is a member of the superfamily of membrane-bound heme-copper oxidases (HCOs) which catalyze the reduction of dioxygen to water in the aerobic respiratory chains of prokaryotes and in mitochondria, concomitant with vectorial translocation of protons across the membrane.[2−6] Reduction of dioxygen takes place at a heme-copper site located within a highly conserved subunit (I) consisting of 12 trans-membrane helices, common to all known HCOs. The most extensively studied of these enzymes is cytochrome *c* oxidase (C*c*O) from bovine heart mitochondria. Crystal structures have been reported for several HCOs including several forms of C*c*O,[7−9] cytochromes aa_3 from *Paracoccus denitrificans*[10−12] and *Rhodobacter sphaeriodes*,[13] cytochrome ba_3 from *Thermus thermophilus*,[14] and quinol oxidase bo_3.[15] The structures of the oxidized enzyme reveal an active site (Chart 1) consisting of a heme coordinated by a single histidine residue and a copper ion, Cu_B, liganded by three histidine groups. In C*c*O, the copper ion lies ∼4.9 Å from the heme iron at an angle of ∼13° from the heme normal through the iron. An unexpected feature of the active site, revealed in the C*c*O, *Paracoccus*, and *Thermus* structures, is a covalent bond between one of the Cu_B histidine ligands and a tyrosine residue (H240/Y244, in bovine C*c*O).[9,11,14] This tyrosine residue is hydrogen-bonded to the hydroxy group of the heme a_3 hydroxy-farnesyl side-chain.[7]

In the oxidized forms of all HCOs studied, there is a magnetic coupling between the Fe(III) heme and Cu_B(II) ions. The nature

† School of Chemical Sciences and Pharmacy.
‡ School of Biological Sciences.
§ Present address: School of Cell and Molecular Biosciences, The Medical School, University of Newcastle upon Tyne, Framlington Place, Newcastle, NE2 4HH, U.K.

(1) Abbreviations used: bo_3 = cytochrome bo_3; C*c*O = bovine cytochrome *c* oxidase; EPR = electron paramagnetic resonance; HCO = heme-copper oxidase; MCD = magnetic circular dichroism; VTVF = variable-temperature variable field; SOC = spin−orbit coupling.

(2) Saraste, M. *Q. Rev. Biophys.* **1990**, *23*, 331−366.
(3) van der Oost, J.; de Boer, A. P. N.; de Gier, J. W. L.; Zumft, W. G.; Stouthamer, A. H.; van Spanning, R. J. M. *FEMS Microbiol. Lett.* **1994**, *121*, 1−10.
(4) García-Horsman, J. A.; Barquera, B.; Rumbley, J.; Ma, J.; Gennis, R. B. *J. Bacteriol.* **1994**, *176*, 5587−5600.
(5) Ferguson-Miller, S.; Babcock, G. T. *Chem. Rev.* **1996**, *96*, 2889−2907.
(6) Babcock, G. T.; Wikström, M. *Nature* **1992**, *356*, 301−309.
(7) Tsukihara, T.; Aoyama, H.; Yamashita, E.; Tomizaki, T.; Yamaguchi, H.; Shinzawa-Itoh, K.; Nakashima, R.; Yaono, R.; Yoshikawa, S. *Science* **1995**, *269*, 1069−1074.
(8) Tsukihara, T.; Aoyama, H.; Yamashita, E.; Tomizaki, T.; Yamaguchi, H.; Shinzawa-Itoh, K.; Nakashima, R.; Yaono, R.; Yoshikawa, S. *Science* **1996**, *272*, 1136−1144.
(9) Yoshikawa, S.; Shinzawa-Itoh, K.; Nakashima, R.; Yaono, R.; Yamashita, E.; Inoue, N.; Yao, M.; Fei, M. J.; Libeu, C. P.; Mizushima, T.; Yamaguchi, H.; Tomizaki, T.; Tsukihara, T. *Science* **1998**, *280*, 1723−1729.
(10) Iwata, S.; Ostermeier, C.; Ludwig, B.; Michel, H. *Nature* **1995**, *376*, 660−669.
(11) Ostermeier, C.; Harrenga, A.; Ermler, U.; Michel, H. *Proc. Natl. Acad. Sci. U.S.A.* **1997**, *94*, 10547−10553.
(12) Harrenga, A.; Michel, H. *J. Biol. Chem.* **1999**, *274*, 33296−33299.
(13) Svensson-Ek, M.; Abramson, J.; Larsson, G.; Tornroth, S.; Brezezinski, P.; Iwata, S. *J. Mol. Biol.* **2002**, *321*, 329−339.
(14) Soulimane, T.; Buse, G.; Bourenkov, G. P.; Bartunik, H. D.; Huber, R.; Than, M. E. *EMBO J.* **2000**, *19*, 1766−1776.
(15) Abramson, J.; Riistama, S.; Larsson, G.; Jasaitis, A.; Svensson-Ek, M.; Laakkonen, L.; Puustinen, A.; Iwata, S.; Wikström, M. *Nat. Struct. Biol.* **2000**, *7*, 910−917.

Chart 1. The Active Site of C*c*O (Created from Structure File 2OCC Using a Combination of the Programs MOLSCRIPT[16] and RASTER3D[17])

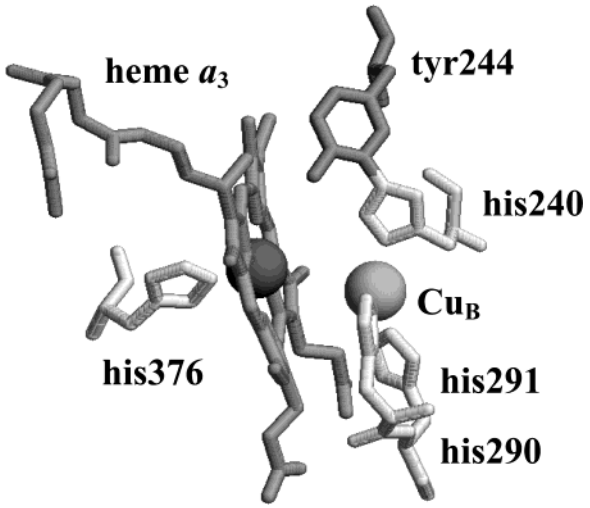

of this interaction has fascinated chemists since Beinert first proposed such a coupling to explain the lack of EPR signals typical of high-spin (HS) Fe(III) heme and Cu(II) from the active site of C*c*O.[18,19] Greenaway et al.[20] subsequently reported that the X-band EPR spectrum of oxidized C*c*O does contain broad features, with unusually short spin−lattice relaxation times, at effective *g*-values of $g' \approx 3$ and ∼12 (originally called $g' = 14$).[21,22] These signals were assigned to the interacting heme-iron and copper pair,[20] but their assignment was ambiguous because early preparations of the enzyme were heterogeneous,[22,23] containing up to four distinct chemical forms of the active site (for a review of this subject, see paper by Moody[24]). Oxidized bo_3 and its fluoride-, chloride-, formate-, and azide-bound forms all display similar, broad X-band EPR features.[25−27] This paper addresses the question of the nature and the strength of the interaction between the two metal ions at the active site of HCOs which results in these broad EPR signals.

Here, we apply both EPR and MCD spectroscopy. *E. coli* bo_3 has particular advantages for MCD studies of the dinuclear site.[28] First, because bo_3 receives electrons from a membrane quinol pool, rather than from soluble cytochrome *c*, it lacks the dinuclear Cu_A site found in subunit II of C*c*O. This simplifies the optical spectrum especially at wavelengths longer than 600 nm, where charge-transfer (CT) bands from the HS Fe(III) heme occur.[29,30] Second, the optical properties of the hemes of bo_3, which compare to those of the protoheme IX class, are far better understood than those of the *a*-type hemes found in C*c*O.[3,31] Both factors allow detailed interpretation of the MCD spectra of bo_3.[27,29]

For the fluoride derivative of bo_3, we showed that the perpendicular and parallel Zeeman mode X-band EPR spectra could be simulated only if spin-coupling between heme o_3 and Cu_B(II) is weak (with $|\mathbf{J}| \approx 1$ cm^{-1}).[32] In this paper, dual-mode X-band EPR spectra of the oxidized and the chloride-, azide-, and formate-bound forms of bo_3 are presented for the first time. These all contain a spectral pattern similar to that observed for the fluoride derivative. We show that the common features of these spectra can only be simulated on the assumption of a weak spin-coupling scheme in which **J** must also be anisotropic. Several of these bo_3 derivatives have also been studied using variable-temperature and variable magnetic field (VTVF) MCD spectroscopy. A new method is described for deconvoluting the heme o_3 MCD contributions in the presence of the more intense bands arising from the second heme in the protein, low-spin (LS) Fe(III) heme *b*. The magnetic field and temperature dependence of the MCD spectra have been analyzed independently of the EPR results. This also shows clearly that the magnetic coupling between heme o_3 and Cu_B in these forms is weak with $|\mathbf{J}| \approx 1$ cm^{-1}. The results from the two techniques provide complementary information because the EPR and MCD spectra are sensitive to different parameters in the spin-Hamiltonian. Within a weak coupling model, where $|D| > |\mathbf{J}|$, the MCD is sensitive to the magnitude of *D*, the axial zero-field parameter of the heme, whereas small changes in **J** are more influential on the form of the EPR spectra. The implications of these findings for the active site structures in the ligand-bound derivatives are discussed.

2. Materials and Methods

2.1. Sample Preparation. bo_3 was isolated from RG145, a previously described overexpressing strain of *E. coli*.[33] For spectroscopic experiments, protein samples were exchanged into 50 mM HEPES, 0.2% (w/v) octyl-β-D-glucopyranoside pH = 7.5. Enzyme concentrations were determined optically using $\epsilon_{406\ nm} = 182$ mM^{-1} cm^{-1} for the oxidized enzyme prior to ligand additions[34] and verified by single integration of the $g = 2.98$ EPR feature of heme *b* against copper(II) EDTA standards using the method of Aasa and Vängärd.[35] All reagents were of analytical grade or better. HEPES, octyl-β-D-glucopyranoside, and the sodium salts of fluoride, formate, chloride, and azide were purchased from Sigma. Ligand-bound derivatives were prepared as previously described to give final ligand concentrations of 20 mM fluoride and formate,[25] 0.5 M chloride,[26,36] and 1 mM azide.[27] For low-temperature MCD measurements, glycerol glassing agent (50%, v/v) was added to the samples.[37]

(16) Kraulis, P. J. *J. Appl. Crystallogr.* **1991**, *24*, 946−950.
(17) Merritt, E. A.; Bacon, D. J. *Methods Enzymol.* **1997**, *277*, 505−524.
(18) Van Gelder, B. F.; Orme-Johnson, W. H.; Hansen, R. E.; Beinert, H. *Proc. Natl. Acad. Sci. U.S.A.* **1967**, *58*, 1073−1079.
(19) Van Gelder, B. F.; Beinert, H. *Biochim. Biophys. Acta* **1969**, *189*, 1−24.
(20) Greenaway, F. T.; Chan, S. H. P.; Vincow, G. *Biochim. Biophys. Acta* **1977**, *490*, 62−68.
(21) Because the *g*-values of these features from non-Kramers systems will be strongly dependent on microwave frequency, we will follow the accepted convention of labeling them as effective *g*-values, g'.[20]
(22) Brudvig, G. W.; Stevens, T. H.; Morse, R. H.; Chan, S. I. *Biochemistry* **1981**, *20*, 3912−3921.
(23) Van Buuren, K. J. H.; Nicholls, P.; Van Gelder, B. F. *Biochim. Biophys. Acta* **1972**, *256*, 258−276.
(24) Moody, A. J. *Biochim. Biophys. Acta* **1996**, *1276*, 6−20.
(25) Watmough, N. J.; Cheesman, M. R.; Gennis, R. B.; Greenwood, C.; Thomson, A. J. *FEBS Lett.* **1993**, *319*, 151−154.
(26) Moody, A. J.; Butler, C. S.; Watmough, N. J.; Thomson, A. J.; Rich, P. R. *Biochem. J.* **1998**, *331*, 459−464.
(27) Little, R. H.; Cheesman, M. R.; Thomson, A. J.; Greenwood, C.; Watmough, N. J. *Biochemistry* **1996**, *35*, 13780−13787.
(28) Watmough, N. J.; Cheesman, M. R.; Butler, C. S.; Little, R. H.; Greenwood, C.; Thomson, A. J. *J. Bioenerg. Biomembr.* **1998**, *30*, 55−62.
(29) Cheesman, M. R.; Watmough, N. J.; Gennis, R. B.; Greenwood, C.; Thomson, A. J. *Eur. J. Biochem.* **1994**, *219*, 595−602.
(30) Thomson, A. J.; Greenwood, C.; Peterson, J.; Barrett, C. P. *J. Inorg. Biochem.* **1986**, *28*, 195−205.
(31) Cheesman, M. R.; Greenwood, C.; Thomson, A. J. *Adv. Inorg. Chem.* **1991**, *36*, 201−255.
(32) Oganesyan, V. S.; Butler, C. S.; Watmough, N. J.; Greenwood, C.; Thomson, A. J.; Cheesman, M. R. *J. Am. Chem. Soc.* **1998**, *120*, 4232−4233.
(33) Au, D. C.; Gennis, R. B. *J. Bacteriol.* **1987**, *169*, 3237−3242.
(34) Cheesman, M. R, Watmough, N. J.; Pires, C. A.; Turner, R.; Brittain, T.; Gennis, R. B.; Greenwood, C.; Thomson, A. J. *Biochem. J.* **1993**, *289*, 709−718.
(35) Aasa, R.; Vänngärd, T. *J. Magn. Reson.* **1975**, *19*, 308−315.
(36) Butler, C. S.; Seward, H. E.; Greenwood, C.; Thomson, A. J. *Biochemistry* **1997**, *36*, 16259−16266.

Chart 2. Energy Level Scheme for the Weak and Strong Coupling Schemes As Described in the Text

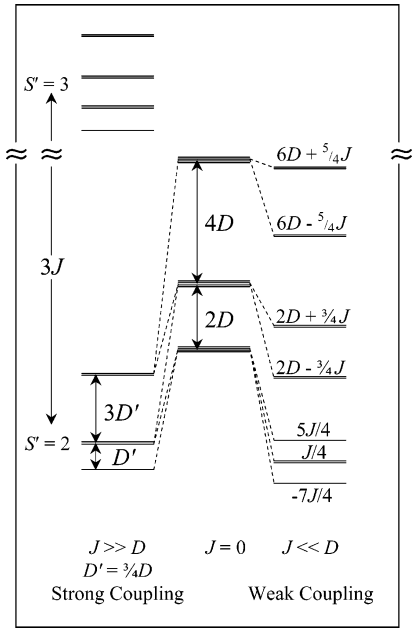

2.2. EPR Spectroscopy. EPR spectra were measured with a Bruker ER300D spectrometer fitted with a dual-mode cavity (type ER4116DM), that can be switched between perpendicular and parallel Zeeman modes by tuning to different frequencies. Perpendicular-mode spectra were obtained at ~9.7 GHz, and parallel-mode spectra were obtained at ~9.4 GHz. These two experimental arrangements differ in the orientation of H_1, the oscillating microwave magnetic field, relative to H_0, the static magnetic field, resulting in transition selection rules of $\Delta M_S = \pm 1$ and $\Delta M_S = 0$, respectively. The instrument is interfaced to a ESP1600 computer (Bruker Analytische Messtechnik GmBH, Silberstreifen, W-7512, Rheinstetten 4, Germany) and equipped with a variable-temperature cryostat and liquid helium transfer line (Oxford Instruments, Osney Mead, Oxford, England).

2.3. MCD Spectroscopy. MCD spectra were recorded on a circular dichrograph, model JASCO J-500D, using an Oxford Instruments SM4 split-coil superconducting solenoid capable of generating magnetic fields up to 5 T.

3. Results

3.1. Exchange Coupling between HS Fe(III) Heme and Cu(II) Ion. The magnetic interaction between HS Fe(III) heme and Cu(II) can be described by an effective spin-Hamiltonian involving an exchange coupling tensor **J**:

$$\hat{H} = [g\beta H\hat{S} + D(\hat{S}_z^2 - \hat{S}^2/3) + E(\hat{S}_x^2 - \hat{S}_y^2)]^{Fe} + [g\beta H\hat{S}]^{Cu} + \hat{S}^{Fe}\cdot\mathbf{J}\cdot\hat{S}^{Cu} \quad (1)$$

where $[\ ]^{Fe}$ is the local spin-Hamiltonian for the $S = {}^5/_2$ heme Fe(III) ion and contains Zeeman, axial (D), and rhombic (E) zero-field splitting terms, respectively. $[\ ]^{Cu}$ is the Zeeman spin-Hamiltonian for the $S = {}^1/_2$ Cu_B(II). Two limiting cases are of interest: the so-called strong coupling scheme, where $|\mathbf{J}| \gg |D|$, and the weak coupling case, when $|\mathbf{J}| \ll |D|$ (see Chart 2). In the former case, the resulting energy levels split into two multiplets of total spin $S' = 2$ and $S' = 3$ which are further split by zero-field terms arising from distortions at the heme. Previous attempts to explain the broad EPR signals[38−41] and the magnetic susceptibility of C*c*O[42−45] have been formulated on this basis. The ground-state multiplet has been assumed to be $S' = 2$ as a result of strong antiferromagnetic coupling. In this case, the system can be described by an effective spin-Hamiltonian in S':

$$\hat{H} = g\beta H\hat{S}' + D'(\hat{S}'_z{}^2 - \hat{S}'^2/3) + E'(\hat{S}'_x{}^2 - \hat{S}'_y{}^2) \quad (2)$$

where D' and E' are now the zero-field splitting parameters of the resultant $S' = 2$ spin-state ($D' = {}^3/_4D$[38]).

In the case of weak coupling, when $|\mathbf{J}| \ll |D|$, the axial zero-field splitting at the heme splits the Fe(III) levels into three Kramers doublets separated in energy by $2D$ and $4D$, respectively, with the lowest doublet having $M_S^{Fe} = \pm{}^1/_2$ and D being typically 5−7 cm^{-1}. Exchange coupling between each of these three Kramers pairs and the single Kramers pair of Cu_B(II) $S = {}^1/_2$ gives rise to three sets of states, each consisting of four levels with the components of the lowest set characterized by M_S values of 0, 0, +1, and −1. EPR transitions between any pair of these sublevels will only be observable experimentally if the energy separation between them in the presence of a magnetic field lies between 0 and 9 GHz and if the selection rules allow for significant intensity. However, the temperature dependence of the MCD intensity of the HS Fe(III) heme transitions will depend both on thermal populations over all levels and on second-order Zeeman mixing. Thus, the two techniques applied together provide a powerful means of determining the wave functions and spin-Hamiltonian parameters. The following sections describe the experimental EPR and MCD data and the theoretical analyses which have been carried out independently for each method.

3.2. EPR Spectra. Figure 1 shows the X-band perpendicular- and parallel-mode EPR spectra of five forms of bo_3 (fluoride, azide, chloride, formate, and oxidized). The spectra were recorded at low temperature (5 K) and high microwave power (103 mW), which saturates the EPR signals at $g = 2.98$, 2.24, 1.50 arising from the magnetically isolated LS Fe(III) heme *b*.[25] For clarity, their positions are indicated on the figure. The narrow, derivative feature from HS Fe(III) heme at $g = 5.8$, observed in each sample, represents only a small fraction (≤5%) of heme which has became uncoupled from Cu_B(II).[32] These two species are half-integer spin, or Kramers systems, and appear in the normal perpendicular mode EPR. These spectra are actually dominated by a series of broad features, with short spin−lattice relaxation times, across the region 0−300 mT. Parallel-mode EPR spectra,[46] for which the oscillating microwave magnetic field is applied parallel to the static field, were also recorded. In this mode, transitions from heme *b* and from HS Fe(III) heme, both simple Kramers systems, are forbidden

(37) Thomson, A. J.; Cheesman, M. R.; George, S. J. *Methods Enzymol.* **1993**, *226*, 199−232.
(38) Hagen, W. R. *Biochim. Biophys. Acta* **1982**, *708*, 82−98.
(39) Dunham, W. R.; Sands, R. H.; Shaw, R. W.; Beinert, H. *Biochim. Biophys. Acta* **1983**, *748*, 73−85.
(40) Hagen, W. R.; Dunham, W. R.; Sands, R. H.; Shaw, R. W.; Beinert, H. *Biochim. Biophys. Acta* **1984**, *765*, 399−402.
(41) Brudvig, G. W.; Morse, R. H.; Chan, S. I. *J. Magn. Reson.* **1986**, *67*, 189−201.
(42) Barnes, Z. K.; Babcock, G. T.; Dye, J. L. *Biochemistry* **1991**, *30*, 7597−7603.
(43) Day, E. D.; Peterson, J.; Sendova, M. S.; Schoonover, J. R.; Palmer, G. *Biochemistry* **1993**, *32*, 7855−7860.
(44) Falk, K. E.; Vänngård, T.; Ångström, J. *FEBS Lett.* **1997**, *75*, 23−27.
(45) Tweedle, M. F.; Wilson, L. J.; Garcia-Iñiguez, L.; Babcock, G. T.; Palmer, G. *J. Biol. Chem.* **1978**, *253*, 8065−8071.
(46) Hendrich, M. P.; Debrunner, P. G. *Biophys. J.* **1989**, *56*, 489−506.

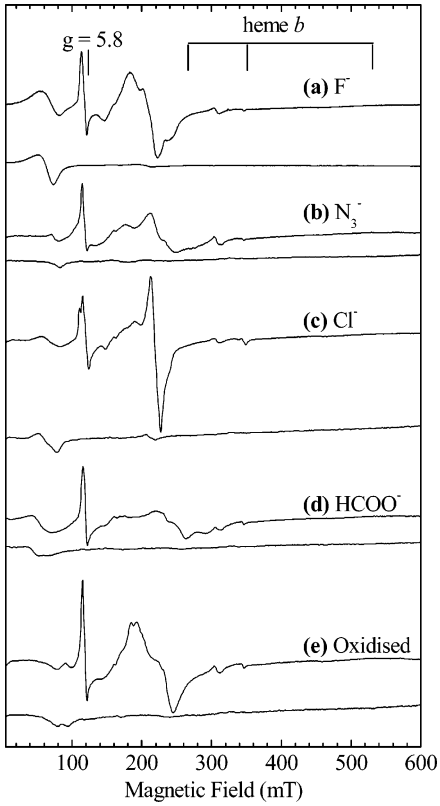

Figure 1. Dual-mode X-band EPR spectra of oxidized bo_3 and adducts. For each, the upper spectrum was recorded in perpendicular mode at 9.7 GHz and the lower was recorded in parallel mode at 9.4 GHz (5 K; 103 mW; modulation, 1 mT; 250 μM).

and hence not observed. In the perpendicular mode, broad signals occur in two regions, low-field at 20−100 mT with a derivative shaped band, the intensity and position of which vary, and a mid-field region at ~150−290 mT with a more complex spectral envelope consisting of a broad derivative which varies in width, intensity, and fine structure. In all five cases, the low-field feature is also detected in parallel mode with an intensity similar to that observed in perpendicular mode, whereas the mid-field signals are absent from parallel mode. Therefore, although the spectra of these five derivatives exhibit differences in intensities and resonance positions, there are characteristics common to all spectra which severely restrict the possible electronic ground-state parameters. We show below, by simulation of EPR spectra which exhibit these characteristics, that the magnitude of **J** can be determined unambiguously.

3.3. Analysis of EPR. A general computer program to simulate EPR spectra in both perpendicular and parallel modes has been described elsewhere.[47] For the case of HS Fe(III) heme o_3 and Cu_B(II), the Hamiltonian of eq 1 has been applied to a basis set comprising products of the single ion spin-functions $|S^{Fe}M_S^{Fe}\rangle|S^{Cu}M_S^{Cu}\rangle$, hereafter abbreviated to $|M_S^{Fe}M_S^{Cu}\rangle$ for $S^{Fe} = {}^5/_2$, $S^{Cu} = {}^1/_2$. The molecular *z*-axis is taken to lie perpendicular to the heme plane. The *g*-values of both metals are set to 2. By varying the magnitude of **J**, we have attempted to simulate dual-mode EPR spectra displaying the characteristics common to the five bo_3 derivatives, specifically two derivative-shaped perpendicular-mode bands in the field regions 20−100 and 160−290 mT, respectively, only the former having intensity in the parallel-mode spectrum, and the ratio of parallel to perpendicular mode intensity at low-field should be <1.7. Simulations have been normalized to experimental spectra by simulation of heme *b* signals in perpendicular mode spectra recorded at 10 K with 2.01 mW microwave power as an internal standard. We have found that the simulation criteria can be satisfied only when $|\mathbf{J}|$ is ~1 cm^{-1} and $D \approx 5$ cm^{-1}. Thus, the weak coupling regime, $J \ll D$, is the appropriate one.

3.4. Four-State Model. In this section, we describe the assignment of the EPR spectra within the four lowest energy levels that arise in the weak coupling limit (Chart 2). The lowest Kramers doublet ($M_S^{Fe} = \pm{}^1/_2$) of the HS Fe(III) heme is separated by 10 cm^{-1} ($2D$) from the $M_S^{Fe} = \pm{}^3/_2$ doublet in an axial zero-field field where $D = 5$ cm^{-1}. An isotropic J of 1 cm^{-1} couples this doublet with the Cu_B(II) $S = {}^1/_2$ Kramers pair, giving four states, in ascending order of energy,

$$|A\rangle = \frac{1}{\sqrt{2}}\left(\left|\frac{1}{2},\frac{-1}{2}\right\rangle - \left|\frac{-1}{2},\frac{1}{2}\right|\right) \qquad M_S = 0$$

$$|B\rangle = -\sin\phi\left|\frac{3}{2},\frac{-1}{2}\right\rangle + \cos\phi\left|\frac{1}{2},\frac{1}{2}\right\rangle \qquad M_S = +1$$

$$|C\rangle = -\sin\phi\left|\frac{-3}{2},\frac{1}{2}\right\rangle + \cos\phi\left|\frac{-1}{2},\frac{-1}{2}\right\rangle \qquad M_S = -1$$

$$|D\rangle = \frac{1}{\sqrt{2}}\left(\left|\frac{1}{2},\frac{-1}{2}\right\rangle + \left|\frac{-1}{2},\frac{1}{2}\right|\right) \qquad M_S = 0 \qquad (3)$$

where $\tan 2\phi = (8)^{1/2}J/(2D - J)$. The degeneracy of $|B\rangle$ and $|C\rangle$ will be further lifted by a rhombic distortion, E, to give two states

$$|B'\rangle = (1/\sqrt{2})(|B\rangle - |C\rangle)$$

and

$$|C\rangle' = (1/\sqrt{2})(|B\rangle + |C\rangle) \qquad (4)$$

Trials with this model show that not only is it necessary to set $|\mathbf{J}| \leq 1$ cm^{-1} and to include a rhombic distortion but that **J** must also be anisotropic with the $\mathbf{J}_z$ component being larger than $\mathbf{J}_x$ and $\mathbf{J}_y$. The effect of this anisotropy is to position one of the energy levels, $|A\rangle$, further from the remaining three, as is illustrated in Figure 2a−c. X-band EPR transitions within the $|B'\rangle$, $|C'\rangle$, and $|D\rangle$ levels, shown by arrows on the figure, then appear in only two magnetic field regions as required. An isotropic **J** would maintain the level $|A\rangle$ close enough to the other three to give rise to a third EPR feature. Simulations thus obtained, using $|\mathbf{J}| \approx 1$ cm^{-1} and anisotropic, are shown in Figure 2d,e. Variations in $|\mathbf{J}|$ of the order of 0.1 cm^{-1} influence the form of the simulation to about the same degree as changes in E/D, and a narrow range of these two parameters can yield satisfactory results. Indeed, a slight increase in the anisotropy of **J** and a complementary change in E/D yields spectra comparable to those in Figure 2, but the assignment of the low- and mid-field features within the $|B'\rangle$, $|C'\rangle$, and $|D\rangle$ levels is reversed. It is not possible to distinguish between these two cases using powder spectra. (See Supporting Information for further details on EPR simulations and assignments.)

In summary, the major features of the dual-mode EPR spectra of all five derivatives of bo_3 have been simulated in terms of a

(47) Hunter, D. J. B.; Oganesyan, V. S.; Salerno, J. C.; Butler, C. S.; Ingledew, W. J.; Thomson, A. J. *Biophys. J.* **2000**, *78*, 439−450.

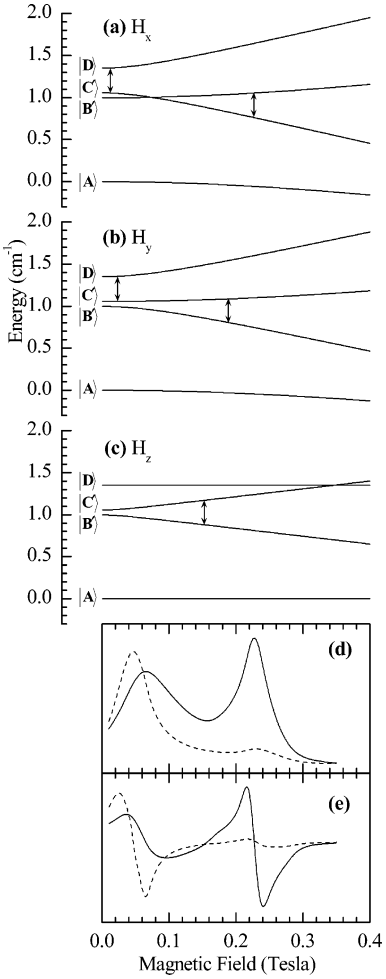

Figure 2. (a−c) Simulations of energy levels with magnetic field parallel to *x*,*y*,*z* axes for the spin-coupled pair, $S_1 = {}^5/_2$ and $S_2 = {}^1/_2$, using the parameters $\mathbf{J} = [-0.5, -0.5, -0.8]$ cm^{-1}, $D = 5$ cm^{-1}, $E/D = 0.035$, $\sigma = 0.15$ cm^{-1}. (d) EPR absorption envelope in the perpendicular (—) and parallel (- - -) modes simulated from energy levels described in (a). (e) Derivative of (d).

four-level scheme in which the spin-coupling between HS Fe(III) heme o_3 and Cu_B(II) is weak ($|\mathbf{J}| \approx 1$ cm^{-1}) and anisotropic. Small changes in the degree of this anisotropy yield two different transition assignments. These differences do not alter the general conclusion concerning the magnitude of **J**. These conclusions are based on the simulation of EPR properties that are common to all of the spectra presented, showing that the same coupling scheme is applicable to all of the bo_3 derivatives, even though there is substantial chemical variation in the nature of the ligand lying between the iron and the copper ions.

3.5. MCD Properties of Hemes *b* and o_3. Although in principle the ground-state electronic properties of the coupled dinuclear site can be extracted from a VTVF MCD study of electronic bands arising from either metal, in practice this entails studying electronic bands arising from HS Fe(III) heme o_3. The electronic transitions of Cu_B(II) are of insufficient intensity both in absorption and in MCD to be detected over a background of much more intense heme bands. In the case of bo_3, however, this approach is further complicated by the presence of the very intense MCD bands of LS Fe(III) heme *b*. Both absorption and MCD spectra show clearly that heme o_3 is HS Fe(III) in all of the derivatives studied here[29] and that heme *b* is LS Fe(III). The MCD spectrum of LS Fe(III) heme at liquid helium temperatures is an order of magnitude more intense than that of HS Fe(III) heme under comparable conditions.

However, Fe(III) heme o_3 gives rise to two MCD CT bands characteristic of the HS state at wavelengths longer than 600 nm which are not overlapped by the intense bands of LS Fe(III) heme *b*.[29] The lower energy CT band (CT_1) is observed at 800−1300 nm in the MCD of a range of HS Fe(III) hemes,[48−50] but being an almost pure porphyrin (π) → Fe(III) (d) CT transition, it is extremely weak. Although it has been observed for several bo_3 derivatives at room temperature,[29] it has insufficient intensity in the low-temperature MCD spectra to be observed above the LS heme *b* CT bands in the same region. The second band, CT_2, appears in the 600−670 nm region and gains appreciable intensity by mixing heavily with the porphyrin $\pi-\pi^*$ transitions at shorter wavelengths.[51] The energies of these $\pi \rightarrow$ d charge-transfer transitions depend directly on d-orbital energies and consequently are sensitive to the nature of the axial ligands. Both CT_1 and CT_2 are derivative-shaped features in the MCD, but, in the presence of LS heme, the CT_2 band is often overlapped to higher energy. However, the negative part of this MCD band to lower energy is usually detectable and, for HS Fe(III) hemes with one histidine ligand, is observed to vary in position from ~660 nm when there is no distal ligand[50] to ~620 nm for distal hydroxide coordination.[52] Other coordination types, such as histidine/H_2O at 630−645 nm, lie between these extremes. The magnetic field and temperature dependence of the HS features in the MCD of bo_3 carry information about the magnetic properties of the dinuclear site. The variable-temperature MCD data can be analyzed to yield a measure of the magnitude of interaction between the metal ions.

A general method of analyzing MCD spectra and magnetization curves of HS metal ions has been presented elsewhere[53] using the application of irreducible tensor methods for simplifying multielectron terms and consideration of spin−orbit coupling (SOC) together with the Zeeman interaction. This gave analytical expressions that parametrize MCD spectra into Gaussian and derivative-shaped bands. The relationship between optical band polarization, the form of the MCD spectra, and of magnetization curves for each transition in the spectrum was described, and symmetry coefficients were tabulated for a HS Fe(III) ion in point symmetry D_{2d}. If, as is the case here, the ground state is $^6A_1$, then these particular coefficients are also valid in C_{4v} symmetry for *xy*-polarized transitions of the type $^6A_1 \rightarrow {}^6E(i)$ and can be used to derive the following equation:

$$\Delta\epsilon({}^6A_1 \rightarrow {}^6E(i)) = -K\frac{1}{h\Delta}\frac{\partial f}{\partial \upsilon}\left(\langle \bar{S}_z \rangle_T C_{f'} + \frac{H\beta}{3}A_{f'}\right)$$

where

$$C_{f'} = \sqrt{\frac{1}{105}}\,|\langle {}^6A_1||m_\perp||{}^6E(i)\rangle|^2 Im(\langle {}^6E(i)||H_{SO}||{}^6E(i)\rangle)$$

(48) Cheng, J. C.; Osborne, G. A.; Stephens, P. J.; Eaton, W. A. *Nature (London)* **1973**, *241*, 193−194.
(49) Cheesman, M. R.; Greenwood, C.; Thomson, A. J. *Adv. Inorg. Chem.* **1991**, *36*, 201−255.
(50) Seward, H. E. T. Ph.D. Thesis, University of East Anglia, 1999.
(51) Braterman, P. S.; Davies, R. C.; Williams, R. J. P. *Adv. Chem. Phys.* **1964**, *7*, 359−407.

$$A_{f'} = \sqrt{\frac{1}{2}}\,|\langle {}^6\mathrm{A}_1||m_\perp||{}^6\mathrm{E}(i)\rangle|^2 Im(\langle {}^6\mathrm{E}(i)||L_Z||{}^6\mathrm{E}(i)\rangle) \quad (5)$$

where $C_{f'}$ and $A_{f'}$ represent respectively temperature-dependent and -independent parts as described in detail in ref 53, $\langle||\,||\rangle$ are reduced matrix elements of any operator, and $\langle \bar{S}_k\rangle_T$ is thermally and orientationally averaged in accordance with:

$$\frac{1}{4\pi}\int_0^\pi \int_0^{2\pi} \sum_j \langle S_k\rangle_{jj} \frac{\exp\left(-\frac{E_j}{kT}\right)}{\sum_{j'} \exp\left(-\frac{E_{j'}}{kT}\right)} A_{zk} \sin\theta \, d\theta \, d\phi \quad (6)$$

where $A_{zk} = \cos\theta$, $\sin\theta\cos\phi$, and $\sin\theta\sin\phi$ for $k = z, x, y$.

Here, $\langle S_k\rangle_{jj}$ is the net expectation value of the spin operator component S_k in the ground-state j.

The electronic transitions of both the LS ($S = {}^1/_2$) Fe(III) heme *b* and the HS ($S = {}^5/_2$) Fe(III) heme o_3 are *xy*-polarized throughout the UV−visible and near-infrared regions.[54,55] Both hemes are taken to belong to an effective C_{4v} point group,[54,56] and all of the transitions are ${}^6\mathrm{A}_1 \rightarrow {}^6\mathrm{E}$. Spin−orbit coupling within the excited ${}^6\mathrm{E}$ manifold results in a series of overlapping derivative-shaped temperature-dependent MCD bands (pseudo-A-terms) for both the porphyrin $\pi-\pi^*$ and the CT transitions of heme o_3. Because all of the transitions of both hemes are *xy*-polarized, their MCD temperature and field dependences are wavelength invariant. According to eq 5, the MCD profiles of both hemes are determined by the products of band shape functions and reduced matrix elements. We can therefore describe the overall MCD spectra as a superposition of the following contributions:

$$\Delta\epsilon(\lambda,T,H) = C_{ls}(\lambda)\langle S_z(T,H)\rangle^{ls} + C_{hs}(\lambda)\langle S_z(T,H)\rangle^{hs} + A(\lambda)\frac{\beta H}{3} \quad (7)$$

where $\Delta\epsilon(\lambda,T,H)$ is the total MCD intensity at a specific wavelength, temperature, and magnetic field; the $C_{ls}(\lambda)$ and $C_{hs}(\lambda)$ terms describe the temperature-dependent parts due to heme *b* and heme o_3 respectively; and $A(\lambda)$ represents the temperature-independent contributions from both hemes. The temperature- and field-dependent factor $\langle S_z(T,H)\rangle^{ls}$ for heme *b* can be calculated with the following expression:[57]

$$\langle S_z(T,H)\rangle^{ls} = \frac{1}{4\pi}\int_0^\pi \int_0^{2\pi} g_{zz}\frac{\cos^2\theta\sin\theta}{\Gamma}\tanh\left(-\frac{\beta H}{2kT}\Gamma\right) d\theta\, d\phi \quad (8)$$

where $\Gamma = \sqrt{g_{zz}^2\cos^2\theta + (g_{xx}^2\cos^2\phi + g_{yy}^2\sin^2\phi)\sin^2\theta}$, the g_{ii}-factors being taken directly from the EPR spectra.

Provided that the exchange coupling is small, the optical properties of heme o_3 are unchanged. However, the ground-state magnetic properties are modified, and this will be reflected in the MCD spectra via the temperature- and field-dependent factor $\langle S_z(T,H)\rangle^{hs}$. The latter can be readily calculated by diagonalization of the Hamiltonian matrix constructed from eq 1. The net expectation values of the spin operator S_z^{Fe} for all resulting states are calculated and averaged both thermally and orientationally in accordance with eq 6. The resulting temperature-dependent magnetization curves of heme o_3 MCD bands are sensitive to the parameters of the spin-Hamiltonian.

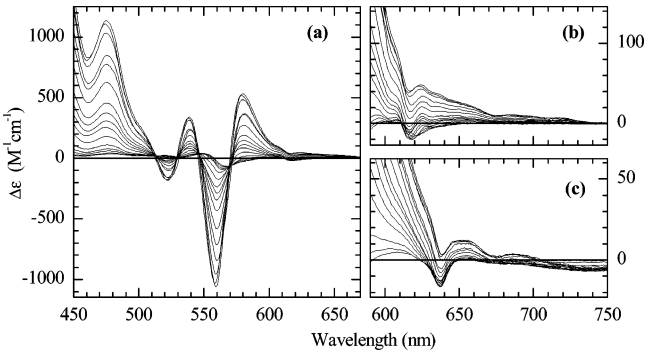

Figure 3. (a) Visible region MCD of fluoride-bound bo_3. Temperatures were 1.80, 2.11, 2.84, 4.20, 5.21, 6.92, 9.99, 13.0, 16.0, 20.0, 29.2, 49.8, 73.1, 110, 161, 200 K. (b) 590−750 nm region expansion of spectra in Figure 4a. (c) 590−750 nm region MCD of azide-bound bo_3. Temperatures were 1.67, 1.81, 2.14, 2.86, 4.21, 4.97, 5.97, 8.21, 10.7, 13.1, 16.0, 20.0, 26.1, 45.1, 68.9, 88.7 K (5 T, 240 μM). All major bands increase with decreasing temperature.

3.6. Experimental MCD Spectra. Figure 3a shows the visible region MCD spectrum of the fluoride derivative of bo_3 measured between 1.6 and 200 K, at 5 T. The spectrum is strongly temperature dependent at all wavelengths, indicating that all of the features arise from paramagnetic chromophores. All features between 450 and 600 nm are typical of LS Fe(III) heme and are due to heme *b*. The variable-temperature MCD spectra have also been recorded for oxidized bo_3 and for two derivatives with azide and formate, respectively, bound at the active site (data not shown). Figure 3b,c shows the region of the MCD between 600 and 700 nm for the fluoride and azide derivatives, respectively. In each case, a distinct minimum, at 616 nm for fluoride and at 637 nm for azide, is observed which is typical of the HS Fe(III) charge-transfer band, CT_2, of heme o_3. As the temperature is increased, all of the heme *b* MCD bands, which dominate Figure 3a, lose intensity with a similar dependence on temperature, showing that they arise from the same chromophore and all have the same (*xy*) optical polarization. However, the CT_2 MCD bands (Figure 3b,c) clearly have a different temperature dependence, becoming more distinct as the temperature is raised to ~20 K, and decreasing in intensity at higher temperatures.

These features contain information about the ground-state magnetic properties. To separate the MCD temperature and field dependence of HS Fe(III) heme from these data, two approaches have been used. The peak-to-trough MCD intensity, $\Delta\epsilon_{VT}$, between 624 and 615.5 nm for the fluoride derivative, and from 646 to 637 nm for the azide derivative, was measured and recorded at a constant magnetic field of 5 T and different temperatures between 1.67 and 100 K. The narrow bandwidth allows observation of the heme o_3 contribution as the intensity of the broader heme *b* tail decreases. However, the heme *b* contribution $C_{ls}(\lambda)\langle S_z(T,H)\rangle^{ls}$ along with $A(\lambda)$, the temperature-independent contribution from both hemes, must now be removed. $\Delta\epsilon_{VT}$ is plotted versus $1/T$ (not shown) and extrapolated to high temperature, $1/T \rightarrow 0$, allowing $A(\lambda)$ to be

(52) Vickery, L.; Nozawa, T.; Sauer, K. *J. Am. Chem. Soc.* **1976**, *98*, 343−350.
(53) Oganesyan, V. S.; George, S. J.; Cheesman, M. R.; Thomson, A. J. *J. Chem. Phys.* **1999**, *110*, 762−777.
(54) Rots, M. I. F.; Zandstra, P. J. *J. Mol. Phys.* **1982**, *46*, 1283−1310.
(55) Smith, D. W.; Williams, R. J. P. *Struct. Bonding* **1970**, *7*, 1.
(56) Oganesyan, V. S.; Sharonov, Y. A. *Biochim. Biophys. Acta* **1998**, *1429*, 163−175.
(57) Thomson, A. J.; Johnson, M. K. *Biochem. J.* **1980**, *191*, 411−420.

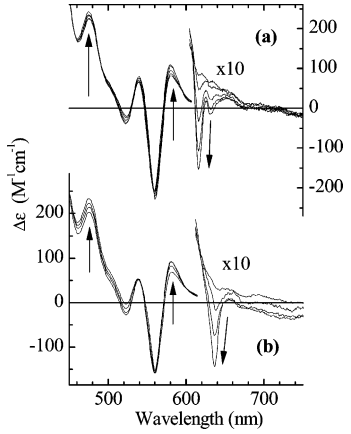

Figure 4. Visible region MCD of (a) fluoride-bound bo_3 and (b) azide-bound bo_3 recorded using constant ratio temperatures and magnetic fields of 1.79 K/0.425 T, 4.23 K/1.00 T, 10.0 K/2.37 T, 16.1 K/3.79 T, 20.0 K/4.74 T for fluoride-bound bo_3 and 1.72 K/0.402 T, 4.26 K/1.00 T, 10.0 K/2.35 T, 20.0 K/4.69 T for azide-bound bo_3. The arrows indicate the direction of change with increasing temperature.

determined and subtracted from the $\Delta\epsilon_{VT}$ data set. The heme *b* contribution to the intensity is removed by the so-called ratio method which exploits the fact that the temperature and field dependences of heme *b* bands are predictable, because $S = {}^1/_2$ MCD intensities vary as $\tanh(-\beta H\Gamma/2kT)$, eq 8. By recording MCD spectra at fixed ratios of H/T, the contribution of heme *b* to the total spectrum remains constant. MCD spectra recorded under this condition are shown in Figure 4 for the fluoride and azide derivatives. Between 450 and 600 nm, where heme *b* features dominate, the spectra show only small differences, attributable to contributions from underlying heme o_3 bands. At wavelengths longer than 600 nm, major changes are observed due to the different field and temperature dependences of the heme o_3 CT_2 bands. From these ratio data (RD), a second CT_2 intensity data set, $\Delta\epsilon_R$, is measured at the same wavelengths used to construct $\Delta\epsilon_{VT}$ from the VT MCD spectra. Because the temperature-independent part (obtained by high-temperature extrapolation of the VT data) has a linear magnetic field dependence, it can be scaled according to the fields used in the RD spectra and subtracted from those spectra to give a corrected set of $\Delta\epsilon_R$. The remaining heme *b* contribution is then eliminated by taking one of the $\Delta\epsilon_R$ points (T_1,H_1) as a reference and subtracting it from the others. Finally, the corrected $\Delta\epsilon_R$ set is normalized to another reference point (T_2,H_2) to give a set of points (T,H) related directly to the intensity factors which are themselves a function of the parameters in the spin-Hamiltonian of eq 1:

$$\frac{\langle S_z(T,H)\rangle^{hs} - \langle S_z(T_1,H_1)\rangle^{hs}}{\langle S_z(T_2,H_2)\rangle^{hs} - \langle S_z(T_1,H_1)\rangle^{hs}} = \frac{\Delta\epsilon_R(T,H) - \Delta\epsilon_R(T_1,H_1)}{\Delta\epsilon_R(T_2,H_2) - \Delta\epsilon_R(T_1,H_1)} \quad (9)$$

where $\Delta\epsilon_R(T,H)$ are now the experimental peak-to-trough MCD RD intensities corrected for the temperature-independent contributions $A(\lambda)$. The experimental data for the fluoride and azide forms are shown as solid circles in Figure 5. The predicted dependence of $\Delta\epsilon_R(T,H)$ on $1/T$ has been calculated for two sets of spin-Hamiltonian parameters. The solid lines show simulations within the weak coupling scheme using $\mathbf{J}_{xyz} = [-0.34, -0.34, -2.30]$ cm^{-1}. The dotted line shows predictions

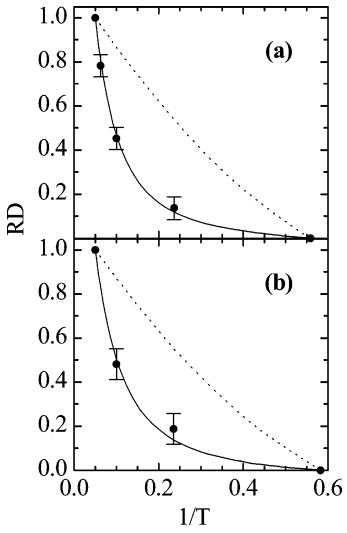

Figure 5. RD plots of the HS Fe(III) heme o_3 CT_2 band intensity extracted from the $\Delta\epsilon_R$ MCD data set as described in the text for (a) fluoride-bound bo_3 and (b) azide-bound bo_3. (●) extracted data points; simulations based on (—) $\mathbf{J}_{xyz} = [-0.34, -0.34, -2.30]$ cm^{-1} and (- - -) the strong coupling parameter set $J = -250$ cm^{-1}, $D' = 0.89$ cm^{-1}, $E/D' = 0.25$.

for the strong coupling regime where $J = 250$ cm^{-1} and $D' = 0.89$ cm^{-1}. Only weak coupling parameters give a fit to the data.

Thus, the RD-MCD approach provides a very clear distinction between the weak and strong coupling regimes, but it also provides the information essential to complete the analysis of the $\Delta\epsilon_{VT}$ data. The $\Delta\epsilon_R$ data set is acquired within the restriction of a fixed H/T ratio. The magnetic field used at the lowest attainable temperature (~1.7 K) is chosen so as to give an acceptable signal intensity. In practice, this dictates that, at the maximum field (5 T), the appropriate temperature is ~20 K. The $\Delta\epsilon_{VT}$ data which can be recorded over a wider temperature range (1.7−200 K) constitute a larger data set and provide an additional route to determining the magnitude of the ZFS and *J* parameters. Fitting the RD curves of Figure 5 yields a value for $(C^{hs}(\lambda_2) - C^{hs}(\lambda_1))$ in the term for heme o_3 intensity in eq 7. The corresponding value for heme *b*, $(C^{ls}(\lambda_2) - C^{ls}(\lambda_1))$, is provided by the invariant part of the RD-MCD intensity in the $\Delta\epsilon_R$ data set. This can, in turn, be used to fix the LS heme *b* contribution in the expression for the VT MCD intensity,

$$\Delta\epsilon_{VT}(T,H) = (C^{ls}(\lambda_2) - C^{ls}(\lambda_1))\langle S_z(T,H)\rangle^{ls} + (C^{hs}(\lambda_2) - C^{hs}(\lambda_1))\langle S_z(T,H)\rangle^{hs} \quad (10)$$

The $\Delta\epsilon_{VT}(T,H)$ data can then be simulated, again using the parameters of eq 1. Figure 6 shows, for the fluoride and azide bo_3 derivatives, plots of the $\Delta\epsilon_{VT}(T,H)$ data set (solid circles) against $1/T$ measured at 5 T plus simulations (solid lines). The magnitudes of the individual contributions to the simulated curve from the LS (- - -) and HS (·····) heme terms of eq 10 are also shown (they are actually of opposite signs). Figure 6a also show a composite curve derived from the strong coupling (-·-·-) parameter set $J = 250$ cm^{-1}, $D' = 0.89$ cm^{-1}, $E'/D' = 0.25$. Slight improvements to the agreement are achieved by minor changes to D and E/D as detailed in the figure legends. Thus, the MCD analysis is in agreement with the EPR conclusions that $|\mathbf{J}| \approx 1$ cm^{-1} but complements the EPR in being more sensitive to variations in D and E rather than in $\mathbf{J}$ itself.

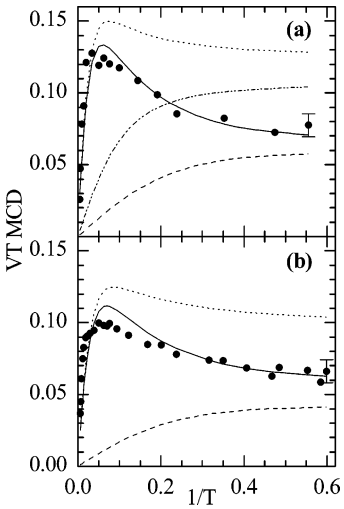

Figure 6. HS Fe(III) heme o_3 Ct_2 band intensity extracted from the $\Delta\epsilon_{VT}$ MCD data set for (a) fluoride-bound bo_3 and (b) azide-bound bo_3. (●) data points; (- - -) simulated LS Fe(III) heme *b* contribution, (·····) simulated contribution from the coupled active site using $D = 5$ cm^{-1}, $E/D = 0.06$, $\mathbf{J}_{xyz} = [-0.34, -0.34, -2.30]$ cm^{-1} (fluoride) and $D = 4.2$ cm^{-1}, $E/D = 0.04$, $\mathbf{J}_{xyz} = [-0.34, -0.34, -2.30]$ cm^{-1} (azide); (—) sum of these two contributions. In (a), (·····) simulated sum of heme *b* contribution plus that derived from a strong coupling parameter set $J = -250$ cm^{-1}, $D' = 0.89$ cm^{-1}, $E/D = 0.25$.

4. Discussion

We have probed the ground-state magnetic parameters of the active site, spin-coupled pair, HS Fe(III) heme o_3 and Cu_B(II), in *E. coli* HCO, bo_3, using both parallel and perpendicular mode X-band EPR and VTVF MCD spectroscopy. The EPR properties of the active site in the oxidized, fluoride, azide, and formate forms have been studied in detail. Despite having different ligands bound at the heme-copper site, the EPR spectra of all four derivatives are remarkably similar, showing broad signals in two regions with effective g'-values of ~12 and ~3. Both signals have intensity in the perpendicular EPR mode, but only the former has significant intensity in the parallel mode. These distinctive features of the EPR spectra have been successfully simulated using a model of weak anisotropic exchange coupling ($|J| \approx 1$ cm^{-1}) between high-spin ferric heme o_3 and Cu_B(II). All transitions arise from within the four lowest levels with effective $M_S = 0, 0, +1, -1$, the highest and lowest of which are separated by $\sim 3\sqrt{2}J$ in zero field. The assignment of the two groups of EPR transitions within this four-level scheme is not unambiguous. For example, either the signal at $g' \approx 12$ can occur between the M_S +1 and −1 levels and the $g \approx 3$ transitions can occur between $M_S = 0$ and +1 or the former can occur between $M_S = 0$ and +1 and the latter between +1 and −1. The assignments can only be settled definitively by experiments on oriented samples. Although we do not have such data on oriented bo_3, we have reported EPR spectra of oriented samples of C*c*O and shown that the $g = 12$ signal arises from transitions between $M_S = 0$ and +1.[47]

VTVF MCD spectra has been used to determine the ground-state magnetic parameters of the dinuclear metal site of two adducts of bo_3, with fluoride and azide. The VT-MCD of the oxidized and formate-bound bo_3 is of a similar form, consistent with the general conclusion that $|J| \approx 1$ cm^{-1} (data not shown). The MCD was used to probe the porphyrin-to-Fe(III) CT_2 band of heme o_3 between 600 and 650 nm. Although this region is overlapped by a broad tail of intense LS Fe(III) heme *b* bands, by collecting MCD at magnetic fields and temperatures selected to ensure that the heme *b* contributions remain invariant, we have been able to separate the contributions from the LS and HS hemes. Analysis of the VT-MCD curves of heme o_3 in terms of two coupling models, with $|J| \approx 1$ cm^{-1} and $|J| \approx 250$ cm^{-1}, shows unambiguously that *J* must lie in the former regime with a heme *D*-value of ~5 cm^{-1}. Although the MCD spectra are sensitive to *J*, rather than to the anisotropy in *J*, when it is small, they are also sensitive to the value of *D*. Thus, the analyses carried out by EPR and MCD are complementary, enabling different sets of spin-Hamiltonian parameter to be determined accurately. However, both techniques do depend on the magnitude of *J* and clearly demonstrate that *J* must be much smaller than *D* and cannot lie in the region range $J \gg D$. The *J*-value must also be anisotropic to obtain a good description of the EPR spectra.

The conclusions from this work, of a weakly coupled pair, are different from those drawn from many studies over the last 30 years of the magnetic properties of the heme-copper site in the form of bovine C*c*O which gives rise to the $g' = 12$ signals. Because crystallographic studies of the oxidized forms of bo_3 and C*c*O show remarkably similar structures for both active sites, these apparent differences between the magnetic properties require explanation. We have, therefore, reexamined earlier interpretations of the EPR spectra and magnetic susceptibility data for C*c*O. We can show, indeed, that they are all consistent with the weakly coupled model put forward here for bo_3.

Previous Studies. A number of previous EPR studies have assigned the broad $g' = 12$ signals. For example, in a pioneering use of parallel-mode EPR measurements, Hagen assigned this signal to a transition within the $M_{S'} = \pm 2$ non-Kramers doublet of an $S' = 2$ system arising from strong ($|J| > 100$ cm^{-1}) antiferromagnetic coupling of Cu_B(II) to HS Fe(III) heme a_3.[38] It was, however, necessary to use ZFS parameters of $D' = +1.19$ (± 0.16) cm^{-1} and $E'/D' = 0.25$. As Hagen pointed out, D'-values arising from heme axial distortion should be significantly larger than +1.19 cm^{-1} and thus suggested HS ferryl (Fe^{IV}=O) heme a_3 as an alternative origin of the $S' = 2$ species. However, hemes with this oxidation and spin state were, and remain, unknown. Although fast C*c*O may contain an equilibrium mixture of HS and LS Fe(III) heme a_3, it is now generally accepted that, in samples of C*c*O with the characteristic EPR signals, heme a_3 is indeed HS Fe(III).[24,58] Nevertheless, we have tested the appropriateness of this model and parameter set in an attempt to account for the EPR of bo_3. Assuming an $S' = 2$ ground state and using the spin-Hamiltonian, eq 1, with $D' = +1.19$ cm^{-1} after adjustment to the local heme o_3 value of $D = 0.75D' = 0.89$ cm^{-1} and $E'/D' = 0.25$ and with *J* set to an isotropic value of −250 cm^{-1},[38] the $g' = 12$ signal at X-band could be simulated in both perpendicular and parallel mode (see Supporting Information). Yet, significantly, it fails to predict a spectrum of sufficient intensity, or of the correct band shape, in the perpendicular mode. More importantly, it also fails to reproduce the mid-field features observed near $g' \approx 3$ for both the bo_3 derivatives and C*c*O. All of our attempts to simulate these signals within a strong coupling model have proved unsuccessful.

(58) Moody, A. J.; Cooper, C. E.; Rich, P. R. *Biochim. Biophys. Acta* **1991**, *1059*, 189−207.

Many studies of C*c*O by magnetic susceptibility have also been reported.[42−45] Some of the early work may have been bedevilled by the presence of heterogeneity at the active site. Magnetic susceptibility magnetization data, collected from homogeneous preparations of C*c*O showing the broad EPR $g' = 12$ signals, could be fitted to a model of strong exchange coupling within the dinuclear site having a $S' = 2$ system but with $D' = -7$ cm^{-1}, a highly unusual value for the axial zero-field splitting of HS Fe(III) heme.[43] We, therefore, have applied the weak coupling model using parameters drawn from the present work to simulate the saturation magnetization curves reported by Day et al.[43] An excellent fit to the data has been obtained (see Supporting Information). Thus, we conclude that, in this particular case, the susceptibility magnetization data do not allow for a distinction to be made between *J*-values of ∼1 cm^{-1} and several hundred cm^{-1}.

Mössbauer studies on oxidized cytochrome c_1aa_3 from *Thermus thermophilus* revealed multiple, preparation and pH dependent, forms of heme a_3, all spin-coupled to Cu_B(II). The properties of one form of heme a_3, at pH 6.5, could be fitted to either strong or weak ($|J| \approx 1$ cm^{-1}) coupling schemes.[59,60] A broad resonance at $g' \approx 3.3$ in the X-band EPR was assigned to the heme *c*. However, this signal was enhanced by increasing the power to 10 mW, and it shows a strong similarity to the broad bo_3 EPR features.[61]

Effects of Site Heterogeneity. This work seeks to understand how various forms of the active site of oxidized HCOs give rise to broad X-band EPR signals similar to those originally reported, at $g' = 3$ and $g' = 12$, for bovine C*c*O. Early preparations of C*c*O were actually heterogeneous, containing several forms of the oxidized heme-copper site.[24] The broad EPR signals are due to one form only, slow C*c*O, thus-called because of the rate at which it binds ligands such as cyanide ion.[62] Slow C*c*O can be transformed by redox cycling (pulsing) into a fast form which rapidly binds ligands such as CN^- and F^-.[24] Improved preparation methods also yield fast enzyme which has an EPR-silent active site.[63] However, observation of broad EPR signals does not necessarily indicate low activity. Oxidized bo_3 exhibits fast ligand binding and reactivity, yet displays the characteristic EPR. Importantly, the simulated EPR has been normalized to the heme *b* spectrum allowing integration, showing clearly that all of the active site is in the same EPR active form. This eliminates the possibility that activity is due to a subpopulation with an EPR-silent coupled site. Whether the EPR silence of the active site in fast C*c*O is due to small quantitative differences in *J* or to more fundamental structural differences is not known. However, application of the MCD methods described here will be of value in resolving this question and in probing higher heme redox states, such as ferryl (Fe(IV)), implicated in the reaction cycle of cytochrome *c* oxidase.[64,65]

Exchange Pathways and Implications for the Structure of the Active Site. We now examine the implications that $|\mathbf{J}|$ is ∼1 cm^{-1} and anisotropic in all derivatives. Crystal structures of oxidized HCOs show that Cu_B(II) is 4.5−5 Å from Fe(III) and ∼1.8 Å off the heme perpendicular through Fe(III).[7−11,13−15] These distances are too long to allow significant overlap between d-orbitals, and the coupling must be mediated by intervening ligands in a superexchange mechanism. Yet, despite different ligands at the active site, Fe(III)−Cu(II) couplings are very similar. To achive this, certain features must be common to each derivative. These can be illustrated by discussion of the fluoride example. RT-MCD studies indicated that F^- binds directly to heme o_3,[29] but, given the Fe(III)−Cu(II) distance, it is unlikely to bridge between the metal ions. In the fluoride adduct of an inorganic model, where the Fe−Cu distance is 3.96 Å, the F^- is only 1.87 Å from Fe(III) and clearly not a true bridging ligand.[66] For bo_3-fluoride, the exchange coupling was found to be $\mathbf{J}_{xyz} = [-0.34, -0.34, -2.30]$ cm^{-1}, the *z*-axis being the heme perpendicular through Fe(III). These values for $\mathbf{J}_{xyz}$ correspond to an isotropic contribution of −0.99 cm^{-1} and anisotropic components of $\mathbf{J}_{anis} = [0.65, 0.65, -1.31]$ cm^{-1}.

Chart 3. The Exchange Coupling Pathways for the Anisotropic Contributions to **J** As Described in the Text

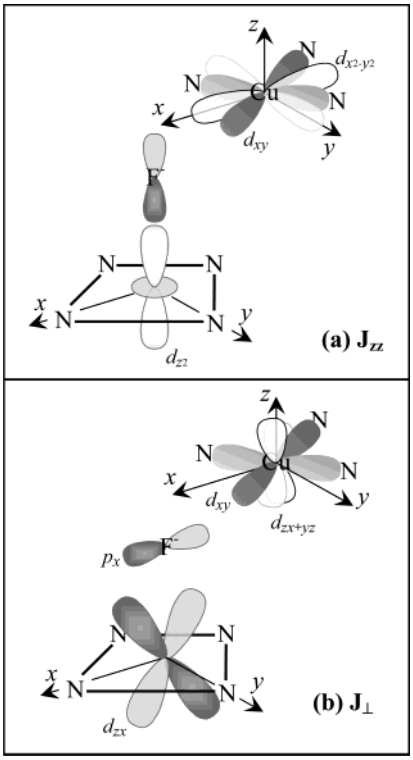

All five d-orbitals of HS Fe(III) are magnetic and cannot contribute to anisotropy.[67] Mixing of Cu_B(II) d-orbitals by spin−orbit coupling (SOC) must therefore be the source of exchange anisotropy, and the pathway between the metals must involve one of the formally nonmagnetic orbitals of Cu_B(II). Coupling via the magnetic orbital would result in a larger isotropic **J**. Chart 3 illustrates one way in which this might occur. Cu_B(II) is liganded by three histidine nitrogens in a plane approximately parallel to the heme with Cu_B displaced from the *z*-axis. In a

(59) Rusnak, F. M.; Münck, E.; Nitsche, C. I.; Zimmerman, B. H.; Fee, J. A. *J. Biol. Chem.* **1987**, *262*, 16328−16332.
(60) Kent, T. A.; Münck, E.; Dunham, W. R.; Filter, W. F.; Findling, K. L.; Yoshida, T.; Fee, J. A. *J. Biol. Chem.* **1982**, *257*, 12489−12492.
(61) Fee, J. A.; Choc, M. G.; Findling, K. L.; Lorence, R.; Yoshida, T. *Proc. Natl. Acad. Sci. U.S.A.* **1980**, *77*, 147−151.
(62) Baker, G. T.; Noguchi, M.; Palmer, G. *J. Biol. Chem.* **1987**, *262*, 596−604.
(63) Palmer, G.; Baker, G. M.; Noguchi, M. *Chem. Scr.* **1988**, *28A*, 41−46.
(64) Fabian, M.; Palmer, G. *Biochemistry* **1999**, *38*, 6270−6275.
(65) Morgan, J. E.; Verkhovsky, M. I.; Palmer, G.; Wikström, M. *Biochemistry* **2001**, *40*, 6882−6892.
(66) Lee, S. C.; Holm, R. H. *J. Am. Chem. Soc.* **1993**, *115*, 5833−5834.
(67) Moriya, T. *Phys. Rev.* **1960**, *120*, 91−99.

coordinate system collinear with that of the heme, the magnetic orbital of $Cu_B(II)$, $3d_{xy}$, is directed toward the ligating N atoms. The p-orbitals F^- provide effective overlap with the magnetic orbitals of Fe(III). As shown, the $Cu_B(II)$ $3d_{xy}$ would not overlap effectively with F^- p-orbitals, resulting in a negligible exchange interaction, perhaps represented by the observed small isotropic contribution to J. In contrast, the nonmagnetic $Cu_B(II)$ orbitals $3d_{x^2-y^2}$ and $(3d_{zx} \pm 3d_{yz})$ are positioned potentially to provide effective overlap with F^- p-orbitals. Mixing of $Cu_B(II)$ d-orbitals by SOC transfers spin density from $3d_{xy}$ into these formally nonmagnetic orbitals, contributing to exchange coupling between copper and iron via the J_{zz} and $J_\perp$ terms, respectively. Thus, the coupling, which results from second-order SOC, is smaller in magnitude than might be anticipated for direct overlap of magnetic orbitals and is also anisotropic (see Supporting Information for additional comments). The weak couplings indicate that overlap of magnetic orbitals is severely hindered in all of these forms of bo_3. This suggests a high degree of structural similarity, and the long Fe−Cu distance may also be a common feature. In a series of inorganic models of the dinuclear site, in which the metal ions are separated by oxo, hydroxo, or F^- ions, the Fe−Cu distance is much shorter, 3.6−3.8 Å. With formate and acetate bridges, the separation increases. All are strongly antiferromagnetically coupled to give $S' = 2$ ground states. None give rise to X-band EPR spectra.[66,68−73]

The long Fe−Cu separation may have mechanistic implications. Most model complexes have short Fe−Cu distances, <4 Å, and in the reduced state react with oxygen to form a peroxo species, $Fe(III)-O_2^{2-}-Cu_B(II)$.[74−77] By contrast, the same reaction in the enzyme leads to a superoxide-containing species in which the copper remains reduced: $Fe(III)-O_2^{-\bullet}-Cu_B(I)$.[78,79] The formation of superoxide has also been reported for a model compound,[80] but one in which the Fe−Cu distance is longer and comparable to that of the enzyme.[81]

The four-level model[30] may have a wider applicability. For example, this model has been adapted to analyze the EPR spectra of and to account for the exchange interaction between an iron−nitrosyl complex, with $S = {}^3/_2$, and semiquinone Q_A^- radical ($S = {}^1/_2$) in Photosystem II.[82] Despite the different nature of the protein complex and the different spin-state of the Fe(III) ion, the features in X-band EPR spectra in both parallel and perpendicular modes are remarkably similar to those observed in the bo_3 derivatives. There are other examples of dual-mode EPR spectra containing the same pattern of bands reported here for the bo_3 adducts. These appear to arise from an $S = {}^5/_2$ Fe(III) heme weakly coupled to a $S = {}^1/_2$ paramagnet. However, in these examples, the second paramagnet appears to be a LS Fe(III) heme: at pH 7.4, the tetraheme cytochrome c_{554}, from *Nitrosomonas europaea*, contains one HS and three LS Fe(III) hemes, as judged by Mössbauer and electronic absorption spectroscopy, and gives rise to the same pattern of EPR spectra as for bo_3;[83] dual-mode EPR spectra almost indistinguishable from those of the bo_3 azide adduct are reported for an octaheme cytochrome isolated from *Desulfuromonas acetoxidans*;[84] and bo_3-fluoride type EPR is found in the pentaheme nitrite reductase, NrfA.[85] Crystallographic structures for NrfA and for cytochrome c_{554} show that both contain a HS heme in close proximity to a LS Fe(III) heme (<4 Å $\pi-\pi$).[85,86]

Acknowledgment. The original impetus for this study came from Prof. C. Greenwood, recently retired from the School of Biological Sciences, U.E.A. We thank him for many helpful discussions. We also thank Prof. R. B. Gennis (Illinois) for supplying genetic constructs and Prof. S. P. J. Albracht (Amsterdam) for help with the initial parallel-mode EPR studies. This work was supported by grant no. BO1727 to CMSB from the U.K. Biotechnology and Biological Research Council (BBSRC) and the U.K. Engineering and Physical Sciences Research Council (EPRSC).

Supporting Information Available: Further details on EPR simulations including those based on previously published parameter sets. Simulation of saturation magnetization data previously reported for C*c*O. Discussion of spin-coupling mechanism (PDF). This material is available free of charge via the Internet at http://pubs.acs.org.

JA038858M

(68) Lee, S. C.; Holm, R. H. *J. Am. Chem. Soc.* **1993**, *115*, 11789−11798.
(69) Karlin, K. D.; Nanthakumar, A.; Fox, S.; Murthy, N. N.; Ravi, N.; Huynh, B. H.; Orosz, R. D.; Day, E. P. *J. Am. Chem. Soc.* **1994**, *116*, 4753−4763.
(70) Scott, M. J.; Zhang, H. H.; Lee, S. C.; Hedman, B.; Hodgson, K. O.; Holm, R. H. *J. Am. Chem. Soc.* **1995**, *117*, 568−569.
(71) Scott, M. J.; Goddard, C. A.; Holm, R. H. *Inorg. Chem.* **1996**, *35*, 2558−2567.
(72) Kauffmann, K. E.; Goddard, C. A.; Zang, Y.; Holm, R. H.; Münck, E. *Inorg. Chem.* **1997**, *36*, 985−993.
(73) Nanthakumar, A.; Fox, S.; Murthy, N. N.; Karlin, K. D. *J. Am. Chem. Soc.* **1997**, *119*, 3898−3906.
(74) Ghiladi, R. A.; Hatwell, K. R.; Karlin, K. D.; Huang, H. W.; Moënne-Loccoz, P.; Krebs, C.; Huynh, B. H.; Marzilli, L. A.; Cotter, R. J.; Kaderli, S.; Zuberbühler, A. D. *J. Am. Chem. Soc.* **2001**, *123*, 6183−6184.
(75) Ghiladi, R. A.; Ju, T. D.; Lee, D. H.; Moënne-Loccoz, P.; Kaderli, S.; Neuhold, Y. M.; Zuberbühler, A. D.; Woods, A. S.; Cotter, R. J.; Karlin, K. D. *J. Am. Chem. Soc.* **1999**, *121*, 9885−9886.
(76) Collman, J. P.; Herrmann, P. C.; Boitrel, B.; Zhang, X.; Eberspacher, T. A.; Fu, L. *J. Am. Chem. Soc.* **1994**, *116*, 9783−9784.
(77) Kopf, M. A.; Karlin, K. D. *Inorg. Chem.* **1999**, *38*, 4922−4923.
(78) Proshlyakov, D. A.; Pressler, M. A.; Babcock, G. T. *Proc. Natl. Acad. Sci. U.S.A.* **1998**, *95*, 8020−8025.
(79) Fabian, M.; Wong, W. W.; Gennis, R. B.; Palmer, G. *Proc. Natl. Acad. Sci. U.S.A.* **1999**, *96*, 13114−13117.
(80) Collman, J. P.; Sunderland, C. J.; Berg, K. E.; Vance, M. A.; Solomon, E. I. *J. Am. Chem. Soc.* **2003**, *125*, 6648−6649.
(81) Collman, J. P.; Sunderland, C. J.; Boulatov, R. *Inorg. Chem.* **2002**, *41*, 2282−2291.
(82) Sanakis, Y.; Petasis, D.; Petrouleas, V.; Hendrich, M. *J. Am. Chem. Soc.* **1999**, *121*, 9155−9164.
(83) Andersson, K. K.; Lipscomb, J. D.; Valentine, M.; Münck, E.; Hooper, A. B. *J. Biol. Chem.* **1986**, *261*, 1126−1138.
(84) Pereira, I. A. C.; Pacheco, I.; Liu, M. Y.; Legall, J.; Xavier, A. V.; Teixeira, M. *Eur. J. Biochem.* **1997**, *248*, 323−328.
(85) Bamford, V. A.; Angove, H. C.; Seward, H. E.; Thomson, A. J.; Cole, J. A.; Butt, J. N.; Hemmings, A. M.; Richardson, D. J. *Biochemistry* **2002**, *41*, 2921−2931.
(86) Iverson, T. M.; Arciero, D. M.; Hsu, B. T.; Logan, M. S. P.; Hooper, A. B.; Rees, D. C. *Nat. Struct. Biol.* **1998**, *5*, 1005−1012.